A thermodynamic analysis of forced convection through porous media using pore scale modeling

Mehrdad Torabi [a], G. P. Peterson [b], Mohsen Torabi [1,b], Nader Karimi [c]

[a] Department of Mechanical Engineering, Islamic Azad University, Central Tehran Branch, Tehran, Iran

[b] The George W. Woodruff School of Mechanical Engineering, Georgia Institute of Technology, Atlanta, GA 30332, USA

[c] School of Engineering, University of Glasgow, G12 8QQ Glasgow, Glasgow, UK

Abstract

The flow thorough porous media is analyzed from a thermodynamic perspective, with a particular focus on the entropy generation inside the porous media, using a pore scale modeling approach. A single representative elementary volume was utilized to reduce the CPU time. Periodic boundary conditions were employed for the vertical boundaries, by re-injecting the velocity and temperature profiles from the outlet to the inlet and iterating. The entropy generation was determined for both circular and square cross-sectional configurations, and the effects of different Reynolds numbers, assuming Darcy and Forchheimer regimes, were also taken into account. Three porosities were evaluated and discussed for each cross-sectional configuration, and streamlines, isothermal lines and the local entropy generation rate contours were determined and compared. The local entropy generation rate contours indicated that the highest entropy generation regions were close to the inlet for low Reynolds flows and near the central cylinder for high Reynolds flows. Increasing Reynolds number from 100 to 200 reveals disturbances in the dimensionless volume averaged entropy generation rate trend that may be due to a change in the fluid flow regime. According to Bejan number evaluation for both cross-section configurations, it is demonstrated that is mainly provoked by the heat transfer irreversibility. A performance evaluation criterion parameter was calculated for different case-studies. By this parameter, conditions for obtaining the least entropy generation and the highest Nusselt number could be achieved simultaneously. Indeed, this parameter utilizes both the first and the second laws of thermodynamics to present the best case-study. According to the performance evaluation criterion, it is indicated that the square cross-section configuration with $\phi = 0.64$ exhibits better thermal performance for low Reynolds number flows. A comparison between the equal porosity cases for two different cross-sectional configurations indicated that the square cross-section demonstrated a higher performance evaluation criterion than the circular cross-section, for a variety of different Reynolds numbers.

Keywords: Entropy generation; Heat transfer; Porous media; Laminar flow; Periodic boundary condition.

1. Corresponding author
Emails: Mohsen.Torabi@my.cityu.edu.hk, torabi_mech@yahoo.com (M. Torabi), Bud.Peterson@gatech.edu (G. P. Peterson).

Nomenclature

A	Surface area of control volume, M^2	N_S	Dimensionless local entropy generation rate, $\frac{S_{gen}D^2\Delta T}{\mu u_D^2}$
T	Temperature, K	N_t	Dimensionless volume-averaged entropy generation rate, $\frac{1}{A}\int_A N_S dA$
D	Circle diameter, Square length, M	Nu	Nusselt number, $\frac{q''D}{k(T_w - T_B)}$
H	REV length scale, M	Ha	Hartman number
k	Fluid conductivity, $\mathrm{W.M^{-1}.K^{-1}}$	Bi	Biot number
S_{gen}	Local entropy generation rate, $\mathrm{W.M^{-3}.K^{-1}}$	Da	Darcy number
u_D	Darcy velocity, $\mathrm{M \cdot s^{-1}}$	**Greek symbols**	
T_w	Wall temperature, K	Φ	Viscous dissipation function, $\mathrm{s^{-2}}$
T_B	Bulk temperature, K	∇	Gradient, $\mathrm{M^{-1}}$
q''	Wall heat flux, $\mathrm{W.M^{-2}}$	ν	Kinematic viscosity, $\mathrm{M^2 \cdot s}$
p	Pressure, $\mathrm{N \cdot M^{-2}}$	μ	Dynamic viscosity, $\mathrm{kg.M.s}$
u_i	Velocity vector, $\mathrm{M \cdot s^{-1}}$	α	Thermal diffusivity, $\mathrm{M \cdot s^{-2}}$
u	X-direction velocity, $\mathrm{M \cdot s^{-1}}$	ϕ	Porosity
v	Y-direction velocity, $\mathrm{M \cdot s^{-1}}$	**Abbreviations**	
x	Flow direction, M	MHD	Magnetohydrodynamic
y	Flow perpendicular direction, M	SIMPLE	Semi-implicit pressure linked equation
ρ	Density, $\mathrm{kg.M^{-3}}$	EGM	Entropy generation minimization
c_p	Specific thermal capacity, $\mathrm{J.kg^{-1}.K^{-1}}$	REV	Representative elementary volume
K	Permeability, $\mathrm{M^2}$	VAT	Volume averaging theory
Re	Reynolds number, $\frac{u_D.D}{\nu}$	LTE	Local thermal equilibrium
Pe	Peclet number, $\frac{\mu c_p}{k}$	LTNE	Local thermal non-equilibrium
Pr	Prandtl number, $\frac{\nu}{\alpha}$	PEC	Performance evaluation criterion
Br	Brinkman number, $\frac{\mu u_D^2}{k(T_w - T_f)}$	HTI	Heat transfer irreversibility
Be_s	Local Bejan number, $\frac{HTI}{HTI + FFI}$	FFI	Fluid friction irreversibility
Be	Bejan number, $\frac{1}{A}\int_A Be_S dA$		

1. Introduction

The investigation of fluid flow in porous media has been of considerable interest for engineers and scientists for several decades. Various applications, such as fluid flow and heat transfer in compact heat exchangers, packed beds, aerosol transport and blood flow in vessels, are all dependent on the behavior of the flow in the porous media [1, 2].

The heat transfer augmentation in thermal systems that utilizes porous media can be evaluated using the second law of thermodynamics. The second law, namely the entropy generation principle, has previously been used to optimize and/or minimize the entropy generation, i.e., exergy destruction, in heat transfer processes. Bejan's pioneering work [3] provided significant insight on the associated relationships. The concept of entropy generation minimization (EGM) [4] was first proposed as an energy-saving approach for thermal processes. Following the initial introduction, a number of investigators extended the concept of entropy generation-based designs to other areas such as thermal/fluid engineering systems [5]. In the present study, a literature review is divided into two categories. First, the investigations related to the entropy generation in free flow and thermal systems are considered, and second, a review related to entropy generation investigations inside porous media is presented.

A number of studies have investigated the entropy generation within fluid flow and thermal systems, but only a relatively few have examined or considered the entropy generation in porous media. Basak et al. [6] studied the entropy generation resulting from free convection inside a cavity using a finite element approach. Different inclination angles, Prandtl numbers and Rayleigh numbers were considered in order to determine the minimal entropy production for each case considered. Torabi et al. [7] investigated the entropy generation between two co-rotating cylinders with a copper-water nanofluid. By applying the analytical solutions, both the local and total entropy generation rates were obtained. The governing equations were found to consist of two energy equations for the inner and outer cylinders, using a constant heat generation, and the energy equation for nanofluid between the cylinders was also considered. A one-dimensional flow equation approach was utilized, assuming a Brinkman viscosity model. In this study, it was concluded that both the local and total entropy generation rates increased as a result of the presence of the nanofluid. This resulted in a temperature reduction within both the solid and fluid media.

In another investigation, Mahian et al. [8] investigated the entropy generation phenomenon in co-rotating cylinders assuming both the magnetohydrodynamic (MHD) and mixed convection effects. Here, the different parameters, such as the Hartman number (Ha), the radius ratio, the mixed convection parameter, and the local and volume averaged entropy generation ratios were considered. It was suggested that the entropy generation reduction, increases with increasing MHD effects and larger spacing between the two cylinders, and results in a lower entropy generation. In a series of papers, Mahian et al. [9, 10] considered the first and the second laws of thermodynamics for nanofluid flow and heat transfer in solar collectors. The investigations discussed the effects of different values of nanoparticle volume fraction, nanoparticle shapes and different relations for thermal conductivity, viscosity and friction factor on the temperature outlet, the Reynolds number (Re), the Nusselt number (Nu), the Prandtl number (Pr), the Bejan number (Be), convection heat transfer coefficient and the entropy generation rate, e.g. heat transfer irreversibility and fluid friction irreversibility. It was observed that for various mass flow rates, the entropy generation rate of steel tubes show higher values compared with the copper tubes Also, the entropy generation rate calculation showed practical importance of tube roughness for high mass flow rates. Mahmud and Fraser [11] surveyed the entropy generation in fundamental steady, forced convection flows such as two-dimensional Poiseuille flow between concentric cylinders, and non-Newtonian fluid flow in tubes and channels. The isothermal and isoflux

boundary conditions were discussed and the entropy generation was determined using the available velocity and temperature profiles. A review about the entropy generation of nanofluid flow including different geometries, e.g. heat exchangers, rotating cylinders and cavities was performed by Mahian et al. [12]. This review gathered numerical and experimental correlations of viscosity, thermal conductivity, specific heat capacity, thermal expansion coefficient and density. The entropy generation investigations of nanofluid in microchannels, channels, tubes and natural and mixed convection systems were thoroughly discussed.

In addition to this work, several investigations were performed to approximate the entropy generation for fluid dynamic systems, such as calculating the entropy generation in turbulent flows. Some of the research was focused on the entropy generation using a Reynolds averaging Navier-Stokes (RANS) approach, such as the so called $k-\varepsilon$ model [13, 14]. Ghasemi et al. [15] compared the performance of different RANS models, in the bypass-transition boundary layer flow using pressure gradient effects. The new transition model, namely the $k-kl-w$ model, was able to predict the entropy generation in turbulent-laminar transition flow far better than other RANS models. Sheikhi et al. [16] applied a large eddy simulation (LES) approach to calculate the entropy generation in mixing flow. Two parallel flows moving toward each other, which became mixed as a unique flow, were considered. The results indicated that the LES approach was capable of predicting the entropy generation for mixing flows in a three-dimensional framework [16].

Investigation of the entropy production in porous media presents a number of interesting aspects and the different physical conditions, and multiplicity of interactions presents some unique challenges. Mahmud and Fraser [17] focused on MHD and free convection effects in Darcy regime for porous flow. Various Rayleigh and Hartman numbers as well as their impacts on the entropy generation and Be were examined. The indicated results showed that increasing the Ha improves the conduction-like heat transfer internal to the flow. As a result, there would is less irregularity in the fluid and thermal systems, decreasing the total entropy generation and the Be. It is important to note that increasing the Rayleigh number increases the entropy generation and heat transfer irreversibility, all of which is concentrated in the central region of cavity. Baytas and Baytas [18] reviewed the entropy generation in porous media. The free convection flow inside a cavity was produced by a heated vertical wall on the right and cold vertical wall on the left, with different inclination angles. The simplified flow governing equations, namely Darcy's equation was used and the Be was calculated for different case studies. Morosuk [19] studied the entropy generation in partially filled porous tubes and channels. The effects of the Darcy number (Da) and porous media thickness were investigated for temperature, velocity and entropy generation fields with isothermal wall boundary conditions. It was found that the maximum entropy generation occurs in the porous and free flow interfaces and that increasing the porous thickness, e.g., decreasing the Da, destroys more available work and produces more entropy.

Alternatively, Betchen and Straatman [20] applied volume averaging operators to the entropy equation and derived a volume averaged entropy generation term. Viscous and thermal contributions of the entropy generation from volume averaged quantities were obtained. The entropy generation and the local thermal non-equilibrium (LTNE) parameter were calculated for a porous medium consisting of highly conductive foams. Mahmud et al. [21] analyzed the heat

transfer and entropy generation in wavy enclosures, assuming a Darcy model. Velocity and temperature distributions were depicted for different Rayleigh numbers and surface waviness. Here, the Be was shown to be Rayleigh-independent for Rayleigh numbers greater than 100 and averaged entropy generation was nearly constant, when the Rayleigh number was less than 10. Yang and Hwang [22] studied the numerical simulation of turbulent fluid flow and heat transfer, for tubes fully and partially filled with a porous material. A standard $k-\varepsilon$ turbulence model for clear fluid flow and a Darcy-Forchheimer model for the porous flow region were formulated. Isothermal and isoflux wall boundary conditions were considered and the effects of various parameters such as the Da, the porous substrate thickness and the Re were presented and discussed. It was concluded that the partially porous tubes demonstrated good performance when the pressure drop and heat transfer were both considered. Finally, the optimum porous region to tube diameter ratio was shown to be approximately 0.8. Mahdavi et al. [23] presented thermal and the entropy generation investigations for partially porous tubes with two conditions; a core porous tube and a wall-adhered porous tube. A finite volume SIMPLER code was used in the numerical approach. Different Darcy numbers, porous thicknesses and thermal conductivity ratios were explored for the Nu calculations. The Da and porous thickness variation impacts on the volume averaged entropy generation and the Be were presented. Interestingly, the measured performance evaluation criterion (PEC) based on the entropy generation suggested that the best heat transfer performance and the least entropy generation occur for the Da of 0.0001 in wall-adhered porous tubes.

Alternatively, other investigations have been utilized to obtain the analytical solutions for the flow, temperature and entropy generation fields in porous media. Tasnim et al. [24] investigated the entropy generation in porous channel flow using MHD, a Darcy model and the local thermal equilibrium (LTE) model for the thermal field. Flow, temperature and the entropy generation distributions for various Ha, the inverse Da and the heat absorption/generation numbers were discussed. Torabi and Zhang [25] explored the entropy generation using numerical-analytical methods in porous channels with a constant magnetic field. Three energy equations using the LTE model were considered; two for solid media, including constant heat generation and one for the fluid flowing through porous media, assuming MHD effects. The local and total entropy generation ratios were examined for various parameters, i.e., the Biot number (Bi), the Da and the Brinkman number. Makinde and Osalusi [26] developed analytical solutions for the flow and thermal fields in a channel with adiabatic and isoflux thermal boundary conditions for the upper and lower walls, respectively. The Darcy model was formulated, neglecting the convection terms in the Navier-Stokes equation. The irreversibility ratio, i.e., the viscous entropy generation as a function of the total entropy generation was discussed for different modified Brinkman numbers. Torabi et al. [27] surveyed the entropy generation in partially porous filled channel flow, using the LTNE model. The numerical-analytical procedure was utilized to determine the velocity and temperature distributions. One-dimensional Darcy-extended flow and creep flow models were utilized for the porous and clear flow regions, respectively. The LTNE modeling results, indicate that the entropy generation consisted of the heat transfer effects between the solid and fluid phases. Ibanez [28] surveyed the slip and convection boundary conditions for flow in a fully porous channel using a constant magnetic field. The flow and temperature fields were analyzed and the magnetic effect was

incorporated into the entropy generation calculation. Various parameters such as the Re, the Eckert number, the Pr, the Ha, the wall slip length, and upper and bottom wall Biot numbers, were examined to optimize the entropy generation rate.

Hooman and Ejlali [29] performed numerical and analytical investigations in fully porous tubes. Velocity, temperature and the entropy generation distributions were derived utilizing a wide range of Darcy numbers. The entropy generation and the Be were depicted, along with the tube radius for different Brinkman numbers. Perturbation analytical methods were shown to be a powerful approach in predicting the energy and entropy generation characteristics of the thermal systems in porous media. Torabi et al. [30] analyzed flow and temperature fields in a partially porous filled channel. Heat generation in both the solid and fluid phases, and constant isoflux wall boundary conditions were considered. The porous medium was attached to the upper and bottom walls and the Darcy-Brinkman momentum equation was used. The effects of the Peclet number, the Da, the dimensionless heat generation in fluid and solid phases and the thermal conductivity ratio were examined for the dimensionless temperature field, the dimensionless velocity field, Nu, the Be, the local entropy generation rate, the volume averaged entropy generation rate and the dimensionless flux ratio. The results indicated that increasing the porous thickness in the channel leads to more entropy generation and the LTNE model was shown to provide a more accurate approach for Nu calculation in porous systems when compared with the LTE model.

As discussed previously, the entropy generation in porous media has been examined from a number of different perspectives, including MHD, wall slip effects, the LTNE, etc. However, there have been a relatively few investigations of the entropy generation in porous media using a pore scale modeling approach. Recently, Betchen and Straatman [31, 32] suggested a new approach of EGM-based design in porous media. The EGM method was employed to optimize a three-dimensional ellipsoid shape to minimize the exergy destruction. It is interesting to note that in this study, the physical parameters, such as the entropy generation or the Nu for thermofluid systems were not discussed.

In the current investigation the flow, temperature, and entropy generation fields in a porous media were developed using pore scale modeling. Both square and circular cross-sectional configurations were considered, and presented as solid obstacles in the computational domain. To incorporate the laminar flow regime, the Dybbs and Edwards [33] classification approach was considered. There are four different regimes that typically exist in porous media: 1) the Darcy regime for $Re < 5-10$, 2) the Forchheimer regime for $5-10 < Re < 150$, 3) the Post-Forchhemeir regime for $150 < Re < 300$, and 4) the chaotic regime for $Re > 300$. Following this classification methodology, the Re varies between 0.01 and 200 to obtain a stable solution with minimal disturbances [34].

The current investigation has been divided into five sections. In section 2, the physical considerations regarding flow, temperature and the entropy generation fields are discussed. In section 3, the governing equations and the normalization procedures are described. In section 4, the computational methods, grid independency, and code

validation study are examined. Section 5 is devoted to the results for flow, temperature and the entropy generation rate fields using flow contours and diagrams. Finally, section 6 presents conclusions regarding the results obtained.

2. Problem formulation

To begin, consider a heat exchanger consisting of similar tubes, and coolant air with constant thermophysical properties, i.e., $k = 0.0242(\frac{W}{M.K})$, $\mu = 1.7894x10^{-5}(\frac{kg}{M.s})$, $c_p = 1004.63(\frac{J}{kg.K})$, $\rho = 1.225(\frac{kg}{M^3})$, flowing between solid matrices, as illustrated in Fig. 1a. In this application, the high temperature bundles of solid surfaces are surrounded by the external flow and the geometry can be replicated for the entire domain. To exploit the periodicity of the geometry, one structural unit can be chosen which represents the entire domain similar to the illustration in Fig. 1b. Using this approach, a single representative elementary volume (REV) of the geometry, using a unit depth and periodic boundary can be used to reduce the time intensive computational processes. The cross-sectional configuration can then be changed to that of a square, as it is shown in Fig. 2. The numerical procedures can account for the length scale, by defining H= 0.1 m. The circular obstacle diameters considered were $D = 0.03$, $D = 0.05$ and $D = 0.06$ m for $\phi = 0.8$, $\phi = 0.6$ and $\phi = 0.4$, respectively. The square cross-section configuration was developed according to the porosity equation, i.e., $\phi = 1 - \frac{D^2}{H^2}$, considering 0.84, 0.64 and 0.51. The Darcy velocity (u_D) and solid matrix diameter (D) were then used to calculate the Re.

3. Mathematical considerations

Steady and incompressible governing equations, namely continuity, momentum and energy equations are written as:

$$\frac{\partial u_j}{\partial x_j} = 0 \tag{1}$$

$$u_j \frac{\partial u_i}{\partial x_j} = -\frac{1}{\rho}\frac{\partial p}{\partial x_i} + \nu \frac{\partial^2 u_i}{\partial x_j \partial x_j} \tag{2}$$

$$u_j \frac{\partial T}{\partial x_j} = \alpha \frac{\partial^2 T}{\partial x_j \partial x_j} \tag{3}$$

The computational processes were performed using the viscous dissipation represented and there was not observed substantial difference with the results without viscous dissipation. In addition, the viscous dissipation, heat generation and radiation effects between the solid and fluid phases are neglected [1].

It should be noted that the heat transfer in porous media could be investigated from two different viewpoints. In the first category, the heat transfer could be evaluated using the volume averaging theory that describes the LTE and the LTNE concepts [35, 22]. Some investigations have examined the heat transfer in porous media using the LTE [25,

36] and others have utilized two distinct energy conservation equations for solid and fluid phases in the porous medium, the so-called LTNE model [27, 37]. In the second category, the heat transfer could be examined using a pore scale modeling approach. In this approach, the heat transfer is investigated between the solid and fluid elements of porous medium [38, 39]. The current investigation utilizes this approach to analyze the illustrated thermal systems in Figs. 1 and 2. In this investigation, the heat transfer between the cylinders and the fluid flow, the Nu utilized is based on the Re. To obtain the appropriate value for this dimensionless parameter, the following relationship was considered:

$$Nu = \frac{q'' D}{k(T_w - T_B)} \tag{4}$$

Equation (4) provides a relationship between the heat transfer effectiveness of the solid and the fluid phases of the system [34], in which $q''(\frac{W}{M^2})$ represents the wall heat flux from the solid matrices to the fluid, and D is the circle diameter or square length. The bulk temperature of the fluid flow was then calculated as:

$$T_B = \frac{\int TudA}{\int udA} \tag{5}$$

The solid obstacle and inlet fluid temperatures were assumed to be 300 K and 200 K, respectively. The thermal field was created using the temperature difference between the incoming cold fluid and the hot cylinders. It should be noted that there are a number of other studies that have utilized a constant temperature wall boundary condition, in the application of the pore scale modeling approach, such as Saito and de Lemos [40] and Matos et al. [41].

The local entropy generation rate equation produced by the velocity and temperature gradients can be written as:

$$S_{gen} = \frac{k}{T^2}(\nabla T)^2 + \frac{\mu}{T}\Phi \tag{6}$$

The first term on the left side of Eq. (6) represents the local entropy generation rate due to the finite temperature difference between fluid particles, e.g., heat transfer irreversibility (HTI) and the second term arises from the resistance force between the individual fluid particles, e.g., fluid friction irreversibility (FFI).

3.1. Normalization

To normalize the conservation equations, the characteristic length scale, velocity, pressure and temperature can be described as follows.

$$x^* = \frac{x}{D} \qquad u^* = \frac{u}{u_D} \qquad p^* = \frac{p}{\frac{\mu u_D}{D}} \qquad T^* = \frac{T - T_B}{T_w - T_B} \tag{7}$$

Substituting the aforementioned parameters in the governing equations, the normalized equations can be represented as:

$$\frac{\partial u_j^*}{\partial x_j^*} = 0 \tag{8}$$

$$u_j^* \frac{\partial u_i^*}{\partial x_j^*} = \frac{1}{Re}\left(-\frac{\partial p^*}{\partial x_i^*} + \frac{\partial^2 u_i^*}{\partial x_j^* \partial x_j^*}\right) \tag{9}$$

$$u_j^* \frac{\partial T^*}{\partial x_j^*} = \frac{1}{Pe}\left(\frac{\partial^2 T^*}{\partial x_j^* \partial x_j^*}\right) \tag{10}$$

respectively. Utilizing the characteristic parameters for the local entropy generation rate, the dimensionless local entropy generation rate can be defined as:

$$N_S = \frac{1}{Br}\left(\frac{\left(\frac{\partial T^*}{\partial x_j^*}\right)}{T^*}\right)^2 + \frac{1}{T^*}\Phi^* \tag{11}$$

The dimensionless local entropy generation rate, the dimensionless volume-averaged entropy generation rate and the normalized viscous dissipation can then be defined as follows, respectively:

$$N_S = \frac{S_{gen} D^2 \Delta T}{\mu u_D^2} \qquad N_t = \frac{1}{A}\int_A N_S dA \qquad \Phi^* = \left(\frac{\partial u^*}{\partial x^*}\right)^2 + \left(\frac{\partial v^*}{\partial y^*}\right)^2 + \frac{1}{2}\left(\frac{\partial u^*}{\partial x^*} + \frac{\partial v^*}{\partial y^*}\right)^2 \tag{12}$$

The dimensionless numbers introduced in the momentum, energy and the local entropy generation rate equations can be defined as:

$$Re = \frac{u_D D}{\nu} \qquad Br = \frac{\mu u_D^2}{k(T_w - T_B)} \qquad Pe = \frac{\mu c_p}{k} \tag{13}$$

The other non-dimensional number for the FFI and the HTI contributions in the entropy generation process is the local Bejan number (Be_s). The Be_s and its volume-averaged, namely Bejan number (Be) are defined as criteria to evaluate the portion of the HTI in the entropy generation [11];

$$Be_s = \frac{HTI}{HTI + FFI} \qquad Be = \frac{1}{A}\int_A Be_S dA \tag{14}$$

It is apparent that for $Be > 0.5$, the entropy is mainly generated by heat transfer that occurs between high and low temperature parts of the system. For $Be < 0.5$ fluid friction, e.g. fluid viscosity, is the main contributor to the entropy generation rate.

4. Solution procedure

The finite-volume commercial code, ANSYS FLUENT 14.0, was used to solve the governing equations. The pressure and velocity fields were decoupled using the SIMPLE algorithm. A second order, upwind scheme was employed to discretize the convection terms. The residuals were reduced to 10^{-7} for the momentum and continuity equations and to 10^{-9} for the energy equation. All calculations were performed with double precision to ensure the accuracy of the results.

The front and back boundaries were specified as periodic, to reproduce the unit structure of a two-dimensional porous medium using the Saito and de Lemos [40] approach. The periodic boundaries were reproduced by re-injecting the temperature and velocity profiles from the outlet to the inlet. Initially, the flow equations were solved and then the after convergence, the energy equations were solved. Next, the velocity and temperature fields were re-injected to the inlet, i.e., the left side of the REV. This procedure was continued until both the inlet and outlet velocity and dimensionless temperature had identical profiles. The temperature can be non-dimensionalized and the temperature profile used to obtain identical profiles between the inlet and outlet conditions. The following correlation was used to normalize the temperature:

$$\left.\frac{T - T_B}{T_w - T_B}\right|_{x=-H} = \left.\frac{T - T_B}{T_w - T_B}\right|_{x=H} \tag{15}$$

Additionally, the symmetry boundary conditions were used for parallel boundaries in the flow direction as:

$$y = -\frac{H}{2} \text{ and } y = \frac{H}{2} \qquad \frac{\partial u}{\partial y} = \frac{\partial v}{\partial y} = \frac{\partial T}{\partial y} = 0 \tag{16}$$

No slip velocity and no jump temperature boundary conditions were employed at the walls, which can be described as:

$$u = v = 0 \qquad T = T_w \tag{17}$$

The aforementioned boundary conditions were normalized using the parameters described in section 3.1. For periodic and symmetry boundaries:

$$T^*\Big|_{x^*=-1} = T^*\Big|_{x^*=1} \tag{18}$$

$$y^* = -\frac{1}{2} \qquad y^* = \frac{1}{2} \qquad \frac{\partial u^*}{\partial y^*} = \frac{\partial v^*}{\partial y^*} = \frac{\partial T^*}{\partial y^*} = 0 \tag{19}$$

Furthermore, the no slip and isothermal wall boundary conditions can be described as:

$$u^* = v^* = 0 \qquad T^* = 1 \tag{20}$$

4.1. Grid independency and code validation

A number of grid independency studies have been performed using quantities such as velocity [19]. It should be noted that each individual study requires that a specific parameter be identified in order to determine the grid independency. As a result, neither the velocity nor the temperature would be appropriate to accommodate the grid independence for the entropy generation. The dimensionless volume-averaged entropy generation rate was selected as the most appropriate parameter for the current investigation. Grid independency was performed for the square cross-sectional configuration, with $Re = 10$ and $\phi = 0.84$. Table 1, illustrates the dimensionless volume-averaged entropy generation rate reduction for a lower node number that reaches a nearly constant value for three of the last mesh of grid independency studies. The difference is 1.2% between 7,800 nodes and 11,000 nodes. The results indicate that 11,000 nodes are sufficient for the current investigation.

For validation, the Nu obtained for the square cross-section configuration in $\phi = 0.84$ was compared with two correlations introduced by Kuwahara et al. [42] and Wakao and Kaguei [43], respectively:

$$Nu = (1 + \frac{4(1-\phi)}{\phi}) + \frac{1}{2}(1-\phi)^{0.5}\, Re_D^{0.6}\, Pr^{\frac{1}{3}} \tag{21}$$

$$Nu = 2 + 1.1 Re_D^{0.6}\, Pr^{\frac{1}{3}} \tag{22}$$

The Nu shows a good agreement with the above correlations as illustrated in Fig. 3. Indeed, the present data fall between the experimental data and several other empirical correlations. Moreover, Fig. 3 shows that the present investigation better predicts the Nusselt numbers when compared with the series solution of Pahor and Strnad [44] and Grosjean et al. [45].

This should be noted that Kuwahara et al. [42] have inspired scholars and researchers for investigating porous media using pore scale modeling approach. However, according to authors' best knowledge, a similar study for the entropy generation and performance evaluation criterion analyses, using square and circular cross-section configurations, has not been performed yet. The current investigation attempts to present a new investigation regarding the entropy generation calculation in porous media and evaluation of different cross-section configurations regarding both the first law and the second law of thermodynamics.

5. Results and discussion

Comprehensive results have been illustrated for both cross-section configurations and can be used to help interpret the quantitative and qualitative data. Seven Reynolds numbers and three porosities were considered for the analyses. By examining the flow and thermal fields, along with the Nu, the N_t, the Be and the PEC, the results can be generalized to a broader range of applications.

5.1. Flow and temperature fields

To achieve more accurate results, the flow and the thermal fields were determined as discussed in section 3. First, the streamlines of both cross-sectional configurations are illustrated and discussed. Then the resulting isothermal lines are presented. The streamlines obtained for the square and circular cross-section configurations are illustrated in Fig. 4, which depicts different Reynolds numbers and porosities. It is apparent here that the streamlines are forced to move forward, with increasing Re. For example, when different porosities are examined, the wake flow is stretched toward the end of the REV, for both the square and circular cross-section configurations. Another consequence of this movement of the streamlines can be seen in the local entropy generation rate contours, which are discussed in section 5.3. One thing that is apparent is that when the flow is in the Darcy regime, the viscous effects are spread out in the REV and this effect does not allow high gradient regions near the windward and the leeward regions of the square.

Having computed the flow filed, the thermal field can then be determined. As seen in Fig. 5, the isothermal lines from the cold fluid could not cover the whole region around the central matrix, for the square cross-sectional configuration, even at $Re = 100$. In fact, by increasing the Re, more interaction between the hot solid and cold fluid is observed, which results in a higher heat transfer between the two phases. For example, observing the isothermal lines for different Reynolds numbers in the square cross-sectional configuration at $\phi = 0.84$, it is apparent that for $Re = 1$ the cold fluid does not have any effect on the high temperature fluid at the back of the cylinder. This effect is enhanced for $Re = 10$ and the flow mostly surrounds the central solid matrix at $Re = 100$. Similarly, the isothermal lines can be interpreted for the circular cross-section configuration. Looking at the isotherms for $\phi = 0.8$ in Fig. 5, it is apparent that the low temperature regions have been more spread in the REV than the square configuration $\phi = 0.84$. For example, there are regions behind the central cylinder for $Re = 1$, that have been affected by the flowing fluid. However, this effect is not seen for $\phi = 0.84$ in the square cross-sectional configuration. If the two fluid flow geometries are considered, it is apparent that the square obstacle produces a wider wake flow, and that the increased velocity and temperature gradients can be attributed to the flow and thermal fields due to the geometric effects of the square cross-section configuration.

5.2. Heat transfer and Nusselt number

A number of investigations have focused on the thermal evaluation of thermofluid systems, e.g., Nu measurement in different geometries with pore scale modeling [46, 34]. The current investigation analyzes the Nu for stable flow

regimes. Regarding the code validation, the correlations of Kuwahara et al. [42] and Wakao and Kaguei [43] were used for the square cross-sectional configuration. For the circular cross-sectional configuration, results of Wakao and Kaguei [43] as well as the correlation suggested by Chen and Wung [47] were utilized to assure the accuracy of results:

$$Nu = 0.78\,Re^{0.45}\,Pr^{0.38} \tag{23}$$

Figures 6 and 7 illustrate the Nu as determined from Eq. (4) for a Re range of 0.01 to 200. It is apparent from Fig. 6, that for the square cross-section configuration, the computational results are closer to those of Wakao and Kaguei [43] than those of Kuwahara et al. [42]. Looking at Fig. 6, it is apparent that the general trend of Nu, e.g., the lower the porosity, the higher the Nu, although for lower Re flows, the Nu decreases with increasing Re. It should be noted that Wakao and Kaguei [43] have collected various data from other investigations and have estimated the trends from different data using Eq. (22). Figure 7 also compares three different solution sets for the Nu in the circular cross-sectional configuration. Examining the trends of the present results, it is apparent that the current results correlate best with those of Wakao and Kaguei [43] and less well with those of Cheng and Wung [47]. This may be due in part to the fact that Chen and Wung [47] assumed a three times larger REV than the assumed REV in the current investigation, and geometrical symmetry was assumed. This could provide a rationale for bifurcating the present study and the reference correlation.

5.3. Entropy generation and Bejan number

Mathematical formulations for the entropy generation rate were described previously in Section 3. Here the calculated results are presented using contours and diagrams, where the contours depict the variation of the local entropy generation rate for different regions of the computational domain. For instance, as shown in Figs. 8 and 9, increasing the Re causes the local entropy generation rate concentration regions to depart from the inlet and migrate to the highly gradient edges of the square and the vertical outlet walls.

Figure 8 depicts the local entropy generation rate contours for the square cross-sectional configuration. As shown, for low Re flows, e.g. $\phi = 0.84$ and $Re = 1$, the majority of the entropy is generated close to the inlet with the other regions contributing very little to the local entropy generation rate. Here, the fluid flows through the voids very slowly and does not produce a shear layer around the square obstacles. However, for higher Re flows the local entropy generation rate contours show a higher concentration close to the square edges and the horizontal walls. Furthermore, if the Re is increased to 100, the majority of the energy loss occurs on the vertical walls of the last matrices. Figure 8 reveals how the local entropy generation rate changes for the Darcy and Forchheimer regimes. Examination of the complex fluid stream and heat transfer, particularly for the square cross-sectional configuration, indicates that the flow impacts the vertical wall and then separates from the edges of the upper and bottom regions of the square where significant gradients for velocity and temperature fields exist. At the horizontal edges of the square, the flow again separates from the surface and behind the square, the wake flow produces a vortex shedding phenomenon that is smoothed out, assuming steady-state conditions. Based upon these findings, it would be

expected that the local entropy generation rate for the square cross-sectional configuration would be greater than for the circular cross-sectional configuration. Figure 9 shows same variations for the local entropy generation rate in the circular cross-sectional configuration. It is important to note that the geometrical variations that the square cross-sectional configuration attributes to the flow are considerably more significant than for the circular cross-sectional configuration, hence the greater value for the local entropy generation rate in the square cross-sectional configuration.

As illustrated in Figs. 8 and 9, the contours do not exhibit same local entropy generation rate for the periodic boundaries. As discussed previously, there are two terms that contribute to the entropy generation rate, namely the viscous dissipation and heat conduction. For the former, the velocity gradient is identical in both the inlet and the outlet, which was prescribed using periodic velocity condition (see Fig. 4). Hence, the temperature at the inlet and outlet should be different, respecting the boundary condition considered in Eq. (15) and contours observed in Fig. 5. Therefore, due to the different temperature at the periodic boundaries, the temperature gradient and consequently, the local entropy generation rates are dissimilar at the inlet and outlet boundaries. However, some of the local entropy generation rate contours demonstrate nearly similar values at the inlet and outlet, which are coordinated with the isothermal contours.

Figures 10 and 11 illustrate how the dimensionless volume-averaged entropy generation rate changes with Re and porosity, for the square and circular cross-sectional configurations, respectively. Both figures indicate that for most of the case studies, increasing the Re and porosity yields an increase in the dimensionless volume-averaged entropy generation rate. However, for higher Re flows, a lower porosity yields an increase in the dimensionless volume-averaged entropy generation rate. This latter statement reveals information about the possible variations that the entropy generation may have for different flow regimes in porous media, such as the Darcy and Forchheimer regimes. For $Re = 100$ flow, both cross-sectional configurations show that the lowest porosity results in the largest dimensionless volume-averaged entropy generation rate. As depicted in Figs. 10 and 11, the dimensionless volume-averaged entropy generation rate increases with Re for medium Re flows. However, some discrepancy in this trend can be observed for higher Re flows, e.g. $Re = 100$. This parameter decreases with reductions in the porosity. In fact, the lower porosity yields a lower value of exergy destruction. This is primarily due to the solid matrix perimeter that increases with reductions in the porosity. When the porosity decreases, there are larger solid obstacles for the fluid flow to pass around. As illustrated in Fig. 5, it is apparent that decreasing the porosity results in less coolant around the hot solids which reduces the temperature gradient between two phases. Therefore, the temperature gradient which is an important factor in the entropy generation is less significant in the lower porosity media. Using the porosity and solid length scale, the permeability can be calculated as follows [48]:

$$K = \frac{D^2 \phi^3}{180(1-\phi)^2} \tag{24}$$

One may consider the square cross-sectional configuration with $\phi = 0.84$ and $\phi = 0.64$ which have $D = 0.04$ and $D = 0.06$, respectively. Substituting the porosity and the square length, the permeability can be calculated as 2.058×10^{-4} and 4.045×10^{-5}, respectively. This demonstrates that increasing the porosity increases the permeability for the present geometries and hence, it can be concluded that increasing porosity, i.e., increasing permeability, increases the dimensionless volume-averaged entropy generation rate.

Figures 12 and 13 show variations of the Be versus different Reynolds numbers by using different porosities. As is observed in Fig. 12, for $\phi = 0.84$ in square cross-section configuration, the HTI dominates over the FFI. This is weakened for lower porosity media and is also decreased for Reynolds numbers between 0.01 and 1, except for the $\phi = 0.64$. Following this trend for the Be, it is observed that the Be increases by increasing the Re to 100. Regarding the aforesaid statements, this may be considered that flow regime transition to a Forchheimer regime, which occurs around $Re = 1$, produces disturbances that augment the FFI contribution in the entropy generation phenomenon. This trend for the Be is also confirmed for circular cross-section configuration, which is seen in Fig. 13. It should be noted that for $Re = 200$, the lower porosity medium results in the higher Be. Therefore, in higher Reynolds flows the FFI effect becomes more pronounced compared with the HTI effect in porous media.

5.4. Performance evaluation criterion (PEC)

Based on the available literature [46, 23], there are two criteria that account for thermal evaluation of porous media between solid matrices and fluid particles. The current investigation emphasizes the importance of the geometric parameters, such as porosity or solid shape, in the thermal performance of thermofluid systems in porous media. For example, Yang et al. [46] considered the pressure gradient as a factor for the heat transfer evaluation. Combining the convection heat transfer coefficient and pressure gradient was considered. Alternatively, Mahdavi et al. [23] investigated porous media from the second law of thermodynamics perspective. The entropy generation number was defined and provided another parameter for approximating the heat transfer capability of thermal systems. Here it was noted that the PEC is the highest for the tubes when the porous materials adhere to walls, including the lowest Darcy number. In fact, the variations in PEC illustrates that different studies utilize this parameter differently. The current study utilizes a new definition of the PEC within the porous media using a pore scale modeling approach to examine both the first and second laws of thermodynamics considerations.

$$PEC = \frac{Nu}{N_t} \tag{25}$$

Figures 14 and 15 show the PEC for the square and circular cross-sectional configurations, respectively. As shown in Fig. 14, the lower porosity results in better thermal performance for Reynolds numbers between 1 and 100. This figure clearly demonstrates that the thermal performance decreases with increasing the Re, and reaches a minimum value approximately around $Re = 200$ and then starts to increase with Re. Interestingly, it can be seen that the PEC is the highest for $\phi = 0.64$. In fact, by looking through Eq. (25) it is apparent that the PEC variation can be governed

purely by the dimensionless volume-averaged entropy generation rate, if the dimensionless volume-averaged entropy generation rate surpasses the *Nu*. This may explain the reverse trends of the PEC versus the Re in Figs. 16-16, when compared with the dimensionless volume-averaged entropy generation rate versus the Re in Figs. 10 and 11.

Figure 16 compares the PEC for the two cross-sectional configurations with different porosities. The highest PEC for flows with $Re<1$ occurs with the square cross-sectional configuration when $\phi=0.64$. Afterwards, the square cross-sectional configuration with $\phi=0.51$ and the circular cross-sectional configuration with $\phi=0.4$ for $10<Re<60$ are observed. The square cross-sectional with $\phi=0.64$ and the circular cross-sectional with $\phi=0.6$ yield better thermal performance than the other cases for $Re=200$. This implies that different porosities should be chosen for different flow regimes, e.g. the Darcy regime or Forchheimer regime, in porous media to lose less exergy.

6. Conclusions

The current investigation examines the first and second laws of thermodynamics in porous media using a pore scale modeling approach. Two cross-sectional configurations, namely a square and circular, and a range of Reynolds numbers were considered for both the Darcy and Forchheimer flow regimes. The flow regimes were chosen to obtain a stable flow with minimal disturbances. Having calculated the Nu for square cross-sectional configuration, the predicted results showed good agreement with the available experimental and empirical data in the literature. Streamlines, isothermal lines, the local entropy generation rate contours, the Nu, the dimensionless volume-averaged entropy generation rate and the performance evaluation criterion have all been investigated for both cross-sectional configurations. The results indicate that increasing the Re and decreasing the porosity produces an increase in the heat transfer. In addition, increasing the Re and going from the Darcy regime to a Forchheimer regime, leads to the local entropy generation rate concentrated regions departure from the inlet. For low Re flows, the entropy is generated close to the inlet of the REV and for higher Re flows, e.g. $Re=100$, the local entropy generation rate contours are more evident on the cylinders' walls. It is interesting to note that the most important regions for the energy loss can be observed through the depicted local entropy generation rate contours. For high Re regimes, one can see the fluid flow colliding with the walls, i.e., the vertical wall of the central cylinder in the square cross-sectional configuration. It is also apparent from the figures that, for the parameter range investigated here, decreasing the porosity increases the Nu. The Be was shown for both cross-section configurations which revealed a dominant effect of heat transfer irreversibility in various Reynolds numbers. However, for some specific Reynolds numbers such as the transition Re from one regime to another regime more contribution of fluid friction irreversibility in the entropy generation phenomenon is observed. A new parameter, namely performance evaluation criterion, has been presented to discuss the thermal performance of the different cases studied. The PEC trend reveals better performance for the lower porosity medium in the low Re flows. In addition, the higher porosity medium such as $\phi=0.64$ for the square cross-section configuration, results in better performance for high Re flows. The current investigation reveals conditions in which the considered thermofluid system, e.g. heat exchanger

fitted with porous media, exhibits the least entropy generation, i.e. exergy destruction, which results in lower energy consumption. Also, there is PEC parameter calculated based on the dimensionless volume-averaged entropy generation rate and Nusselt number which represent the second law of thermodynamics and thermal performance of porous media, respectively. The PEC parameter is able to reveal conditions that thermofluid system destructs least exergy and produces highest thermal interaction between fluid and solid elements. The results may be advantageous for designers and engineers who work in connection with the heat exchanger and cooling electronic packages, in which the optimum space between the elements or the optimum Re can be controlled in order to obtain the best thermal performance.

Acknowledgement

Authors kindly thank Dr. Yosuke Hasegawa from University of Tokyo for his technical comments that improved the level of the present manuscript.

References

[1] Bejan A, Dincer I, Lorente S, Miguel AF, Reis AH. Porous and Complex Flow Structures in Modern Technologies. New York: Springer; 2004.

[2] Ingham DB, Bejan A, Mamut E, Pop I. Emerging Technologies and Techniques in Porous Media. Constanta: Springer; 2004.

[3] Bejan A. A study of entropy generation in fundamental convective heat transfer. J Heat transf 1979;101:718-25.

[4] Bejan A. Entropy generation minimization: the new thermodynamics of finite-size devices and finite-time processes. J Appl Phys 1996;79:1191-218.

[5] Naterer GF, Camberos JA. Entropy-Based Design and Analysis of Fluids Engineering Systems. New York: CRC Press; 2008.

[6] Basak T, Singh AK, Sruthi TPA, Roy S. Finite element simulations on heat flow visualization and entropy generation during natural convection in inclined square cavities. Int Commun Heat Mass Transf 2014;51:1–8.

[7] Zheng N, Liu W, Liu Z, Liu P, Shan F. A numerical study on heat transfer enhancement and the flow structure in a heat exchanger tube with discrete double inclined ribs. App Therm Eng 2015;90:232-41.

[8] Mahian O, Oztop H, Pop I, Mahmud S, Wongwises S. Entropy generation between two vertical cylinders in the presence of MHD flow subjected to constant wall temperature. Int Commun Heat Mass Transf 2013;44:87-92.

[9] Mahian O, Kianifar A, Heris SZ, Wongwises S. First and second laws analysis of a minichannel-based solar collector using boehmite alumina nanofluids: Effects of nanoparticle shape and tube materials. Int J heat mass Transf 2014;78:1166–76.

[10] Mahian O, Kianifar A, Sahin AZ, Wongwises S. Entropy generation during Al_2O_3/water nanofluid flow in a solar collector: Effects of tube roughness, nanoparticle size, and different thermophysical models. Int J heat mass Transf 2014;78:64–75.

[11] Mahmud S, Fraser RA. The second law analysis in fundamental convective heat transfer problems. Int J Therm Sci 2003;42:177–86.

[12] Mahian O, Kianifar A, Kleinstreuer C, A. A-NM, Pop I, Sahin AZ, Wongwises S. A review of entropy generation in nanofluid flow. Int J heat mass Transf 2013;65:514–32.

[13] Kock F, Herwig H. Local entropy production in turbulent shear flows: a high-Reynolds number model with wall functions. Int J heat mass Transf 2004;47:2205-15.

[14] Kock F, Herwig H. Entropy production calculation for turbulent shear flows and their implementation in CFD codes. Int J Heat Fluid Fl 2005;26:672–80.

[15] Ghasemi E, Mceligot DM, Nolan KP, Crepeau J, Tokuhiro A, Budwig RS. Entropy generation in a transitional boundary layer region under the influence of freestream turbulence using transitional RANS models and DNS. Int Commun Heat Mass Transf 2013;41:10-16.

[16] Sheikhi MRH, Safari M, Metghalchi H. Large eddy simulation for local entropy generation analysis of turbulent flows. J Energ Resour 2012;134:041603.

[17] Shohel M, Fraser RA. Magnetohydrodynamic free convection and entropy generation in a square porous cavity. Int J heat mass Transf 2004;47:3245–56.

[18] Baytas AC, Baytas AR. Entropy generation in porous media in Transport Phenomena in Porous Media Volume III. Oxford: Elsevier; 2005.

[19] Morosuk TV. Entropy generation in conduits filled with porous medium totally and partially. Int J heat mass Transf 2005;48:2548-60.

[20] Betchen LJ, Straatman AG. The development of a volume-averaged entropy-generation function for nonequilibrium heat transfer in high-conductivity porous foams. Numer Heat Transf B-Fund 2008;53:412-36.

[21] Shohel M, Fraser RA, Pop I. Flow, thermal, energy transfer, and entropy generation characteristics inside wavy enclosures filled with microstructures. J Heat transf 2007;129:1564-75.

[22] Yang YT, Hwang ML. Numerical simulation of turbulent fluid flow and heat transfer characteristics in heat exchangers fitted with porous media. Int J heat mass Transf 2009;52:2956–65.

[23] Mahdavi M, Saffar-Avval M, Tiari S, Mansoori Z. Entropy generation and heat transfer numerical analysis in pipes partially filled with porous medium. Int J heat mass Transf 2014;79:496–506.

[24] Tasnim SH, Shohel M, Mamun M. Entropy generation in a porous channel with hydromagnetic effect Exergy, an Int J 2002;2:300-08.

[25] Torabi M, Zhang K. Temperature distribution, local and total entropy generation analyses in MHD porous channels with thick walls. Energy 2015;87:540-54.

[26] Makinde OD, Osalusi E. Second law analysis of laminar flow in a channel filled with saturated porous media. Entropy 2005;7:148-60.

[27] Torabi M, Zhang K, Yang G, Wang J, Wu P. Heat transfer and entropy generation analyses in a channel partially filled with porous media using local thermal non-equilibrium model. Energy 2015;82:922-38.

[28] Ibáñez G. Entropy generation in MHD porous channel with hydrodynamic slip and convective boundary conditions. Int J heat mass Transf 2015;80:274-80.

[29] Hooman K, Ejlali A. Entropy generation for forced convection in a porous saturated circular tube with uniform wall temperature. Int Commun Heat Mass Transf 2007;34:408-19.

[30] Torabi M, Karimi N, Zhang K. Heat transfer and second law analyses of forced convection in a channel partially filled by porous media and featuring internal heat sources. Energy 2015;93:106-27.

[31] Betchen LJ, Straatman AG. Entropy generation-based computational geometry optimization of the pore structure of high-conductivity graphite foams for use in enhanced heat transfer devices. Comput Fluids 2014;103:49-70.

[32] Betchen LJ, Straatman AG. A computational method for geometric optimization of enhanced heat transfer devices based upon entropy generation minimization. Int J Numer Meth Fl 2013;71:370–402.

[33] Dybbs A, Edwards RV. A new look at porous media fluid mechanics-Darcy to turbulent in Fundamentals of Transport Phenomena in Porous Media. Netherlands: Springer; 1982.

[34] Gamrat G, Favre-Marinet M, Le Person S. Numerical study of heat transfer over banks of rods in small Reynolds number cross-flow. Int J heat mass Transf 2008;51:853–64.

[35] Baytas AC. Entropy generation for thermal nonequilibrium natural convection with a non-darcy flow model in a porous enclosure filled with a heat-generating solid phase. J Porous Media 2007;10:261–75.

[36] Roy M, Basak T, Roy S. Analysis of entropy generation during mixed convection in porous square cavities: Effect of thermal boundary conditions. Numer Heat Transf A-Appl 2015;68:925-57.

[37] Buonomo B, Manca O, Lauriat G. Forced convection in micro-channels filled with porous media in local thermal non-equilibrium conditions. Int J Therm Sci 2014;77:206-22.

[38] Pathak MG, Mulcahey TI, Ghiaasiaan SM. Conjugate heat transfer during oscillatory laminar flow in porous media. Int J heat mass Transf 2013;66:23-30.

[39] Kim SM, Ghiaasiaan SM. Numerical modeling of laminar pulsating flow in porous media. J Fluids Eng 2009;131:041203.

[40] Saito MB, De Lemos MJS. A correlation for interfacial heat transfer coefficient for turbulent flow over an array of square rods. J Heat transf 2006;128:444-52.

[41] Matos RS, Vargas JVC, Laursen TA, Saboya FEM. Optimization study and heat transfer comparison of staggered circular and elliptic tubes in forced convection. Int J heat mass Transf 2001;44:3953-61.

[42] Kuwahara F, Shirota M, Nakayama A. A numerical study of interfacial convective heat transfer coefficient in two-energy equation model for convection in porous media. Int J heat mass Transf 2001;44:1153-59.

[43] Wakao N, Kaguei S. Heat and Mass Transfer in Packed Beds. New York: Gordon and Breach; 1982.

[44] Pahor S, Strnad J. A note on heat transfer in laminar flow through a gap. Appl Sci Res 1961;10:81-4.

[45] Grosjean CC, Pahor S, Strnad J. Heat transfer in laminar flow through a gap. Appl Sci Res 1963;11:292-94.

[46] Yang J, Wang Q, Zeng M, Nakayama A. Computational study of forced convective heat transfer in structured packed beds with spherical or ellipsoidal particles. Chem Eng Sci 2010;65:726–38.

[47] Chen CJ, Wung TS. Finite analytic solution of convective heat transfer for tube arrays in crossflow: Part ll—heat transfer analisys. J Heat Transf 1989;111:641-48.

[48] Nield DA, Bejan A. Convection in Porous Media. New York: Springer; 2006.

Table 1: The dimensionless volume-averaged entropy generation rate in different grid numbers

Grid	N_t	Error percentage
5000	0.10660139	
7800	0.10374616	%3.8
11000	0.10246321	%1.2

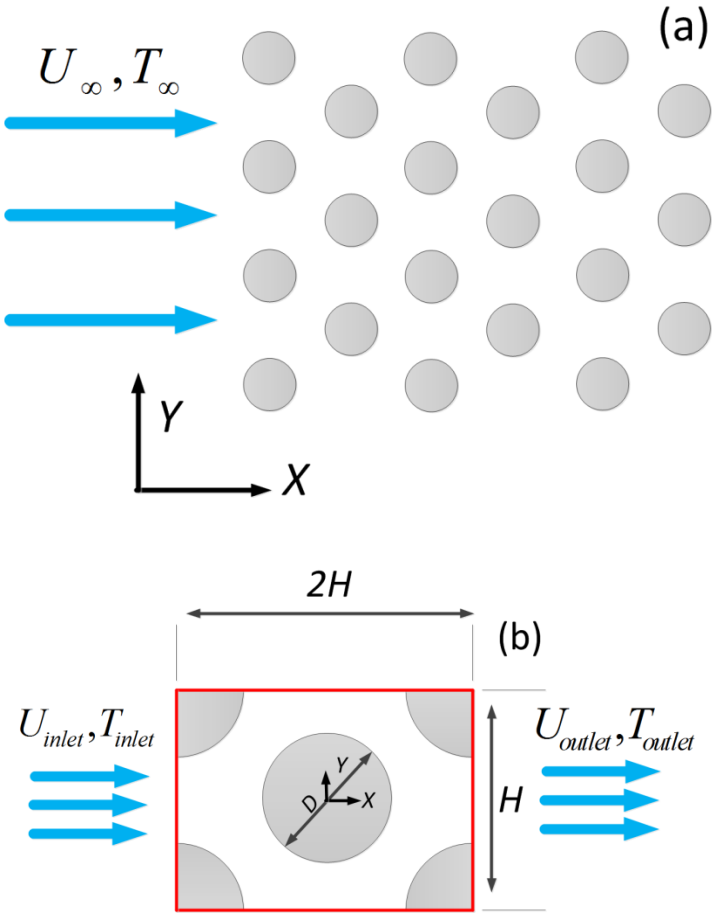

Fig. 1. Geometric model: (a) heat exchanger bundles with circular cross-section configuration,

(b) Structural unit with periodic and symmetry boundaries.

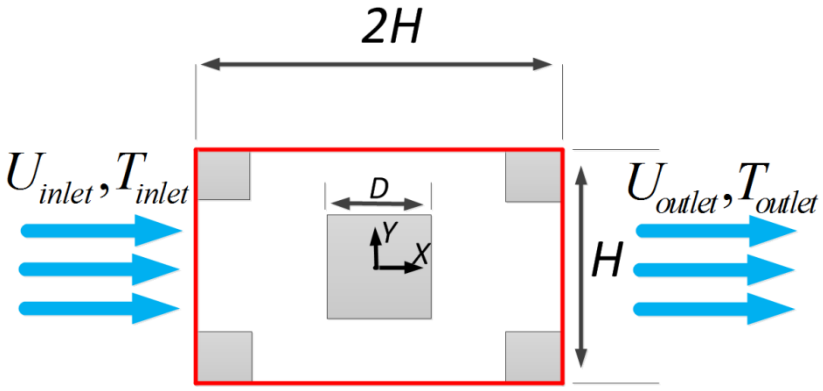

Fig. 2. Geometric model: square cross-section configuration.

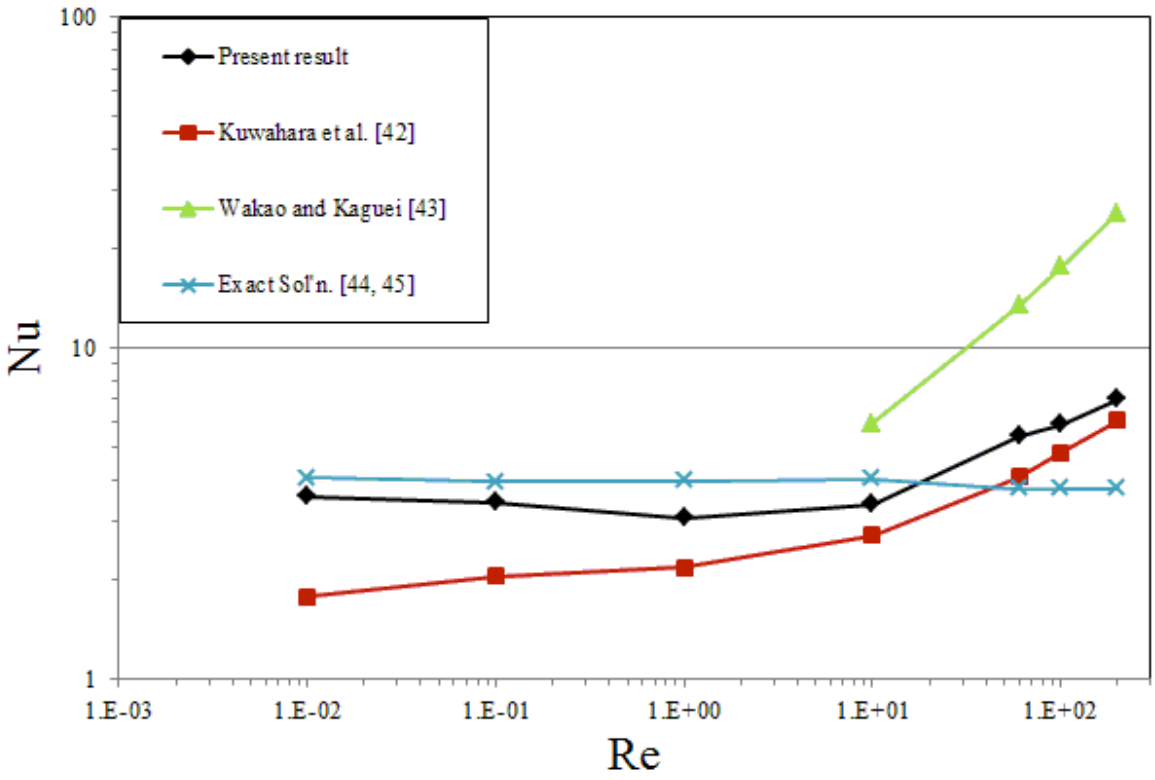

Fig. 3. Code validation for square cross-section configuration in $\phi = 0.84$.

		Re=1	Re=10	Re=100
Square	$\phi = 0.84$	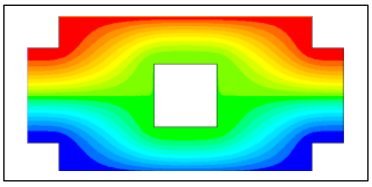	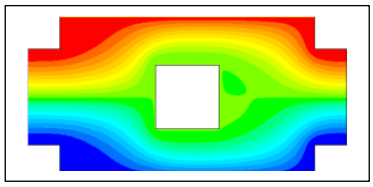	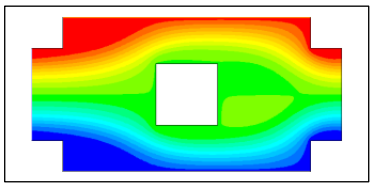
	$\phi = 0.64$	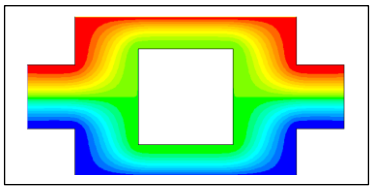	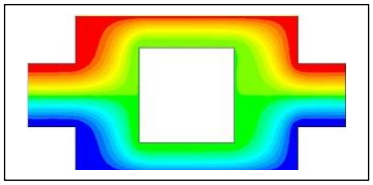	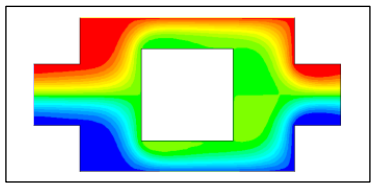
	$\phi = 0.51$	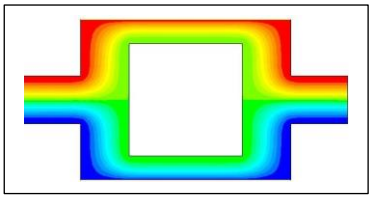	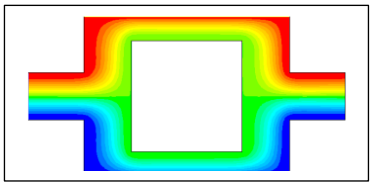	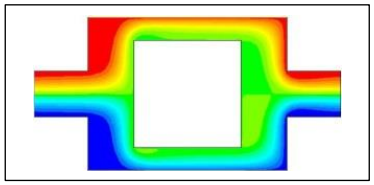
Circle	$\phi = 0.8$	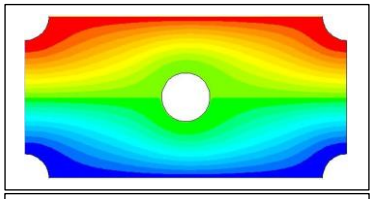	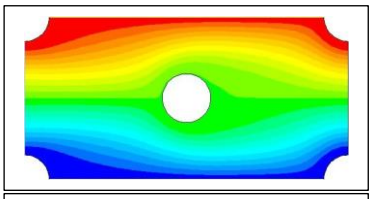	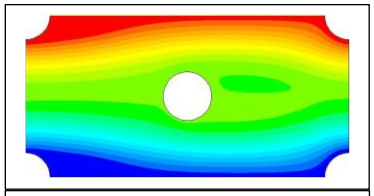
	$\phi = 0.6$	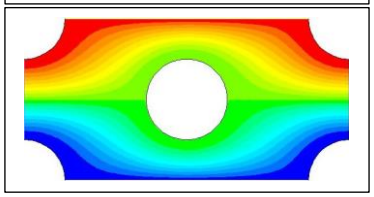	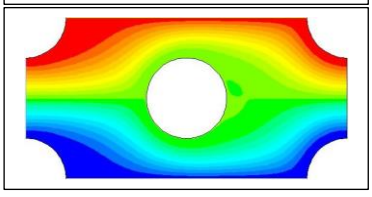	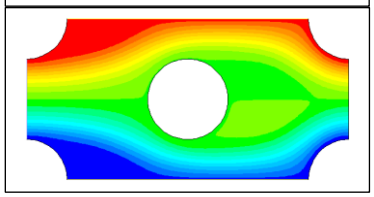
	$\phi = 0.5$	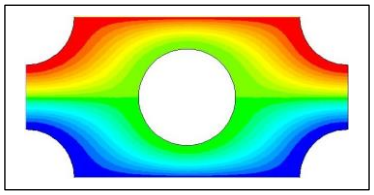	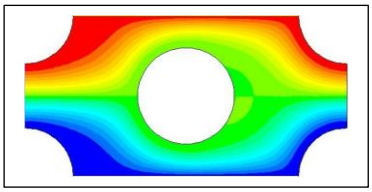	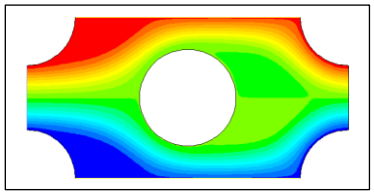

Fig. 4. Streamlines of square and circular cross-section configurations for different Reynolds numbers and porosities.

		Re=1	Re=10	Re=100
Square cross-section configuration	$\phi = 0.84$	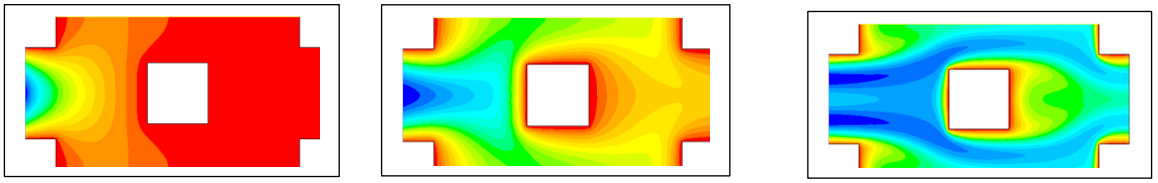		
	$\phi = 0.64$	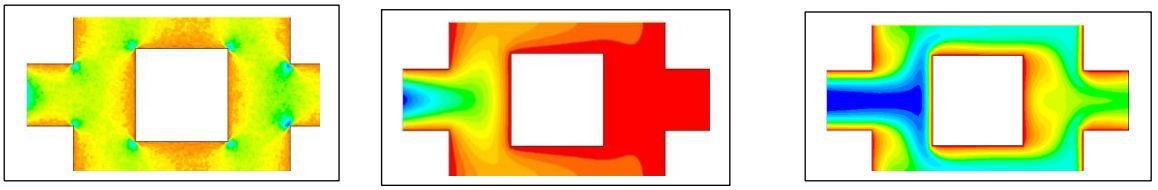		
	$\phi = 0.51$	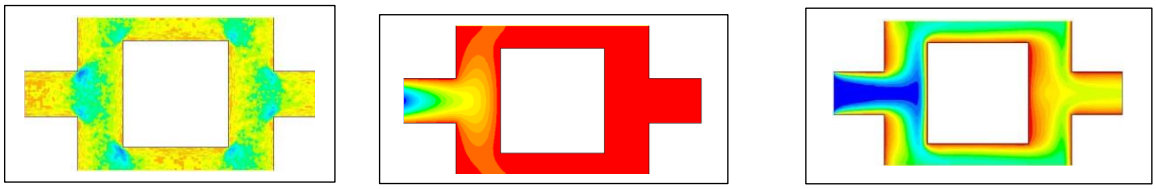		
Circular cross-section configuration	$\phi = 0.8$	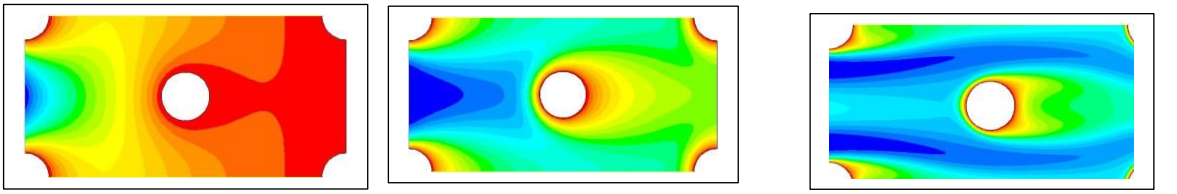		
	$\phi = 0.6$	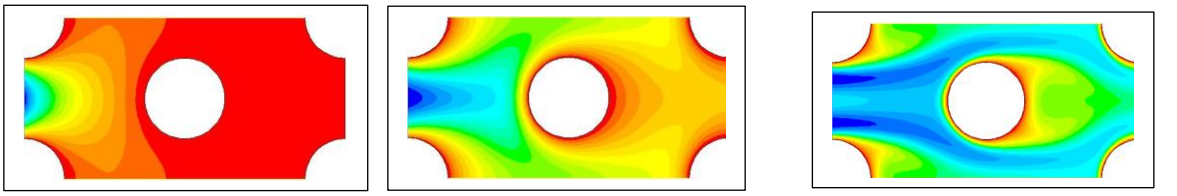		
	$\phi = 0.5$	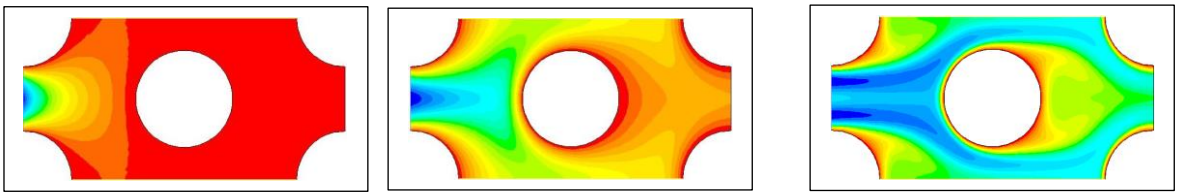		

Fig. 5. Isothermal lines of square and circular cross-section configurations for different Reynolds numbers and porosities.

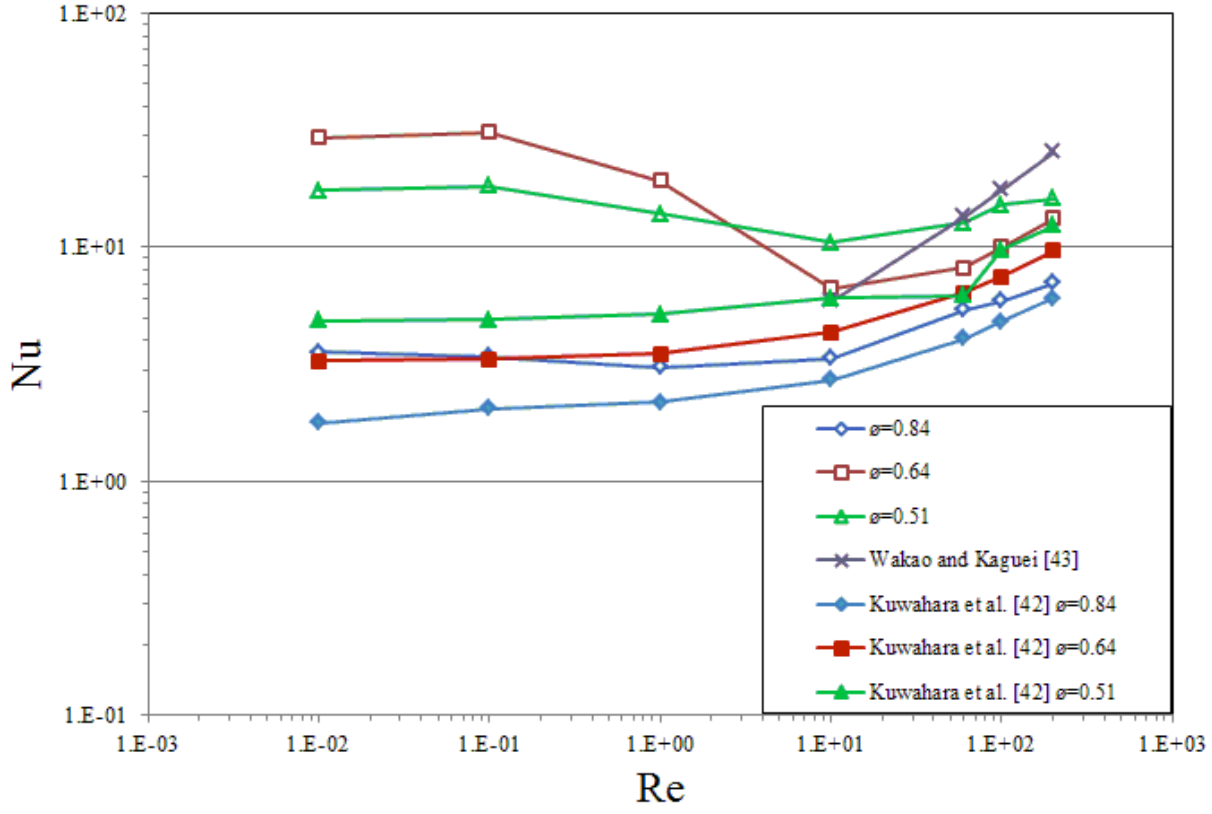

Fig. 6. Nusselt number variations of square cross-section configuration for different Reynolds numbers and porosities.

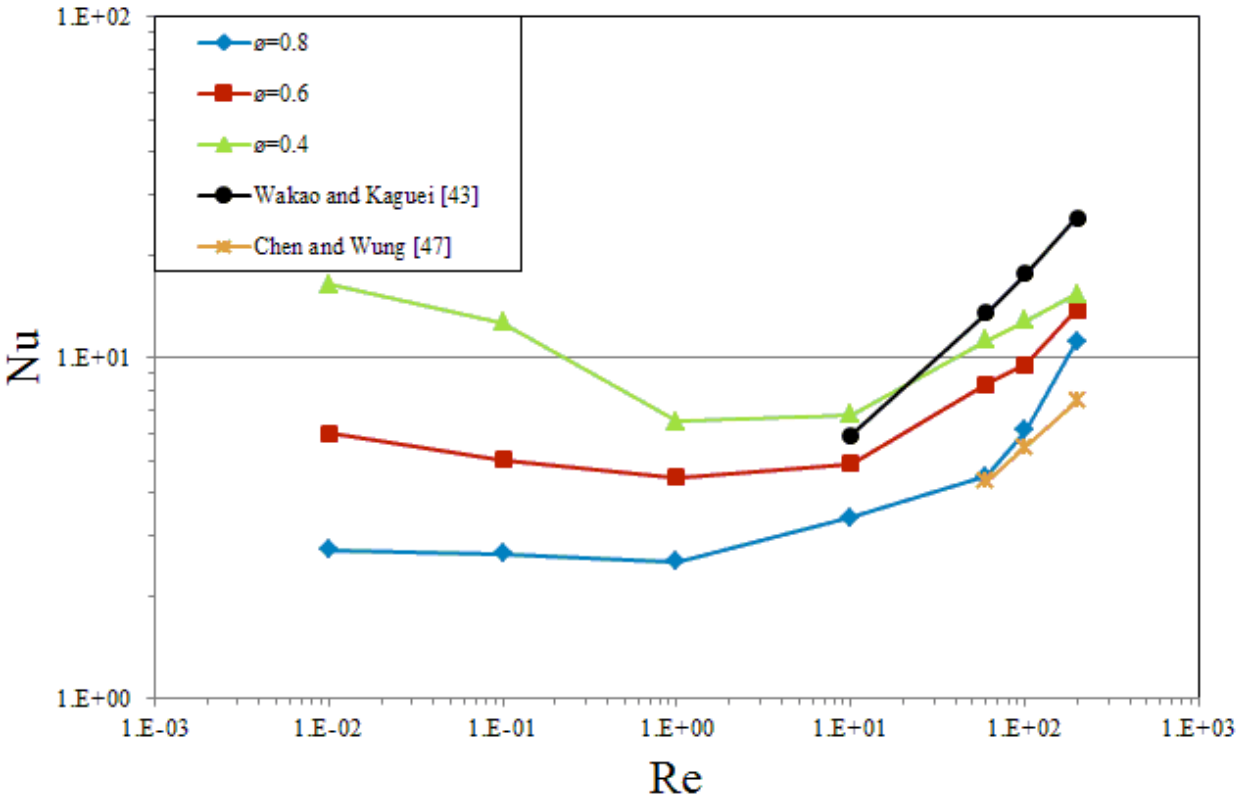

Fig. 7. Nusselt number variations of circular cross-section configuration for different Reynolds numbers and porosities.

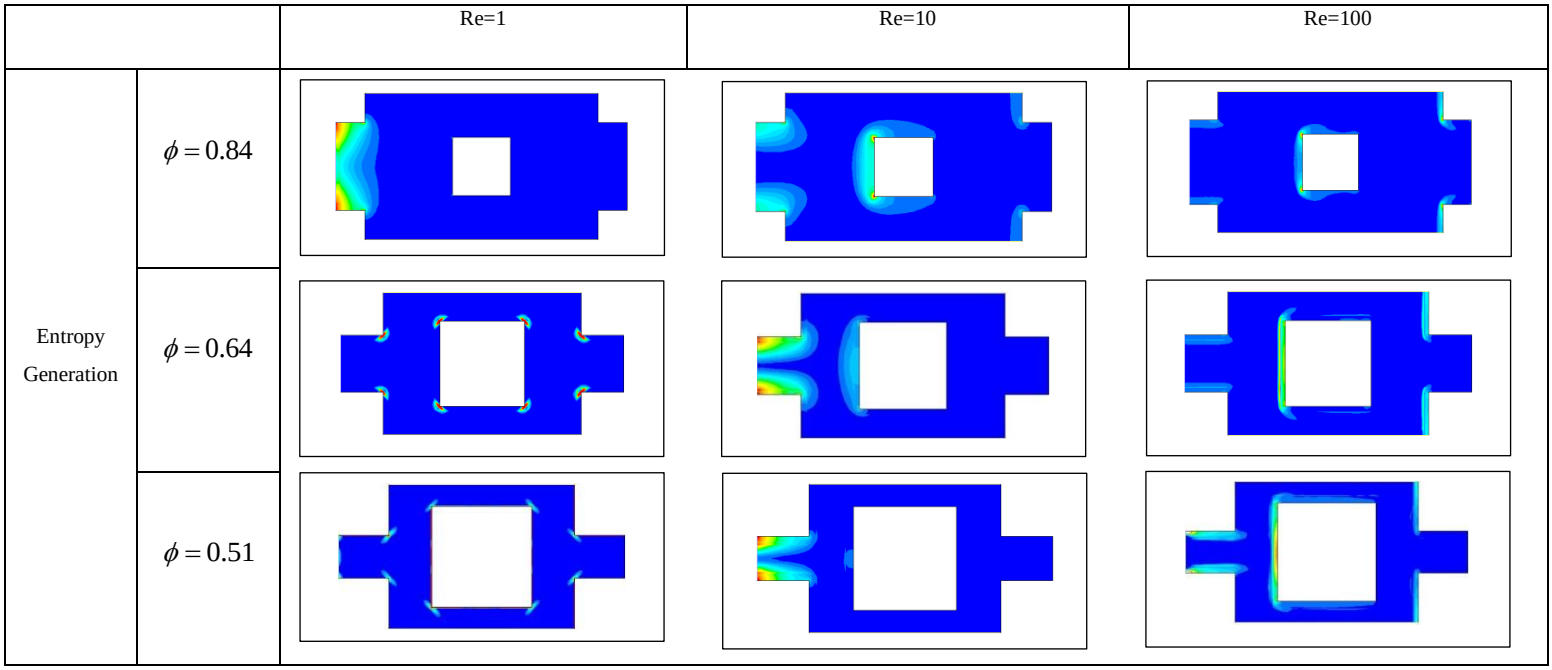

Fig. 8. The local entropy generation rate contours of square cross-section configuration for different Reynolds numbers and porosities.

		Re=1	Re=10	Re=100
Entropy Generation	$\phi = 0.8$	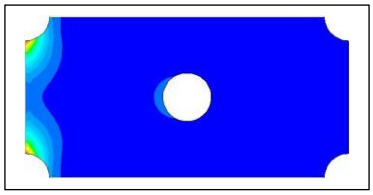	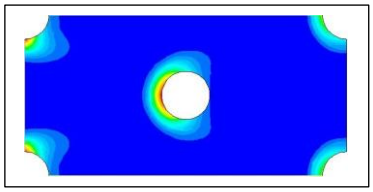	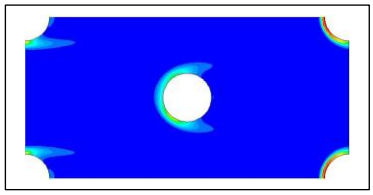
	$\phi = 0.6$	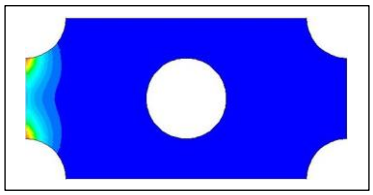	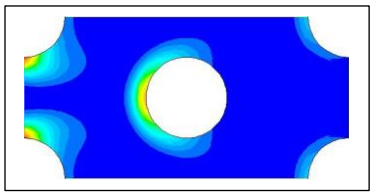	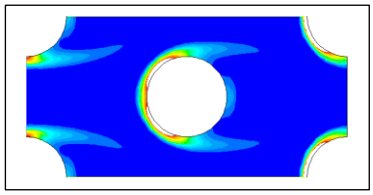
	$\phi = 0.4$	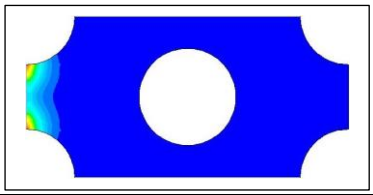	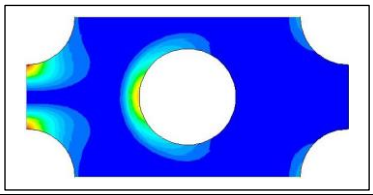	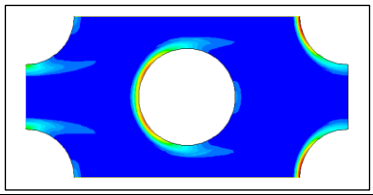

Fig. 9. The local entropy generation rate contours of circular cross-section configuration for different Reynolds numbers and porosities.

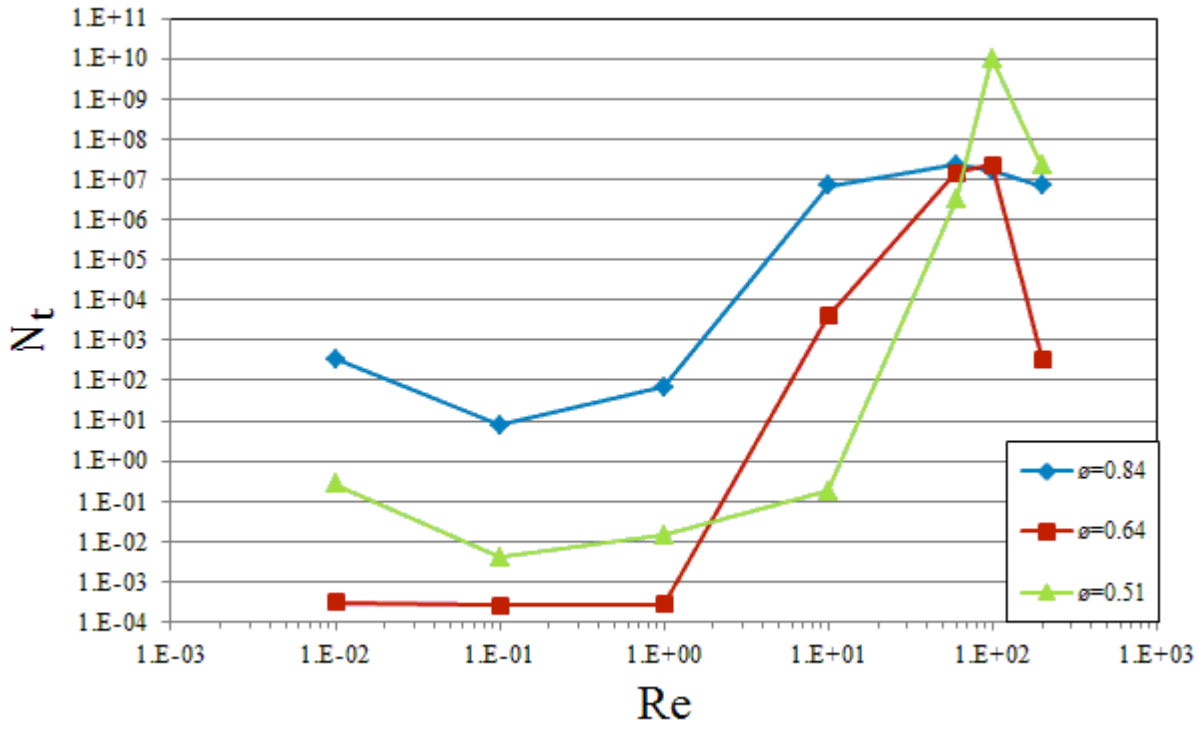

Fig. 10. The N_t variations of square cross-section configuration for different Reynolds numbers and porosities.

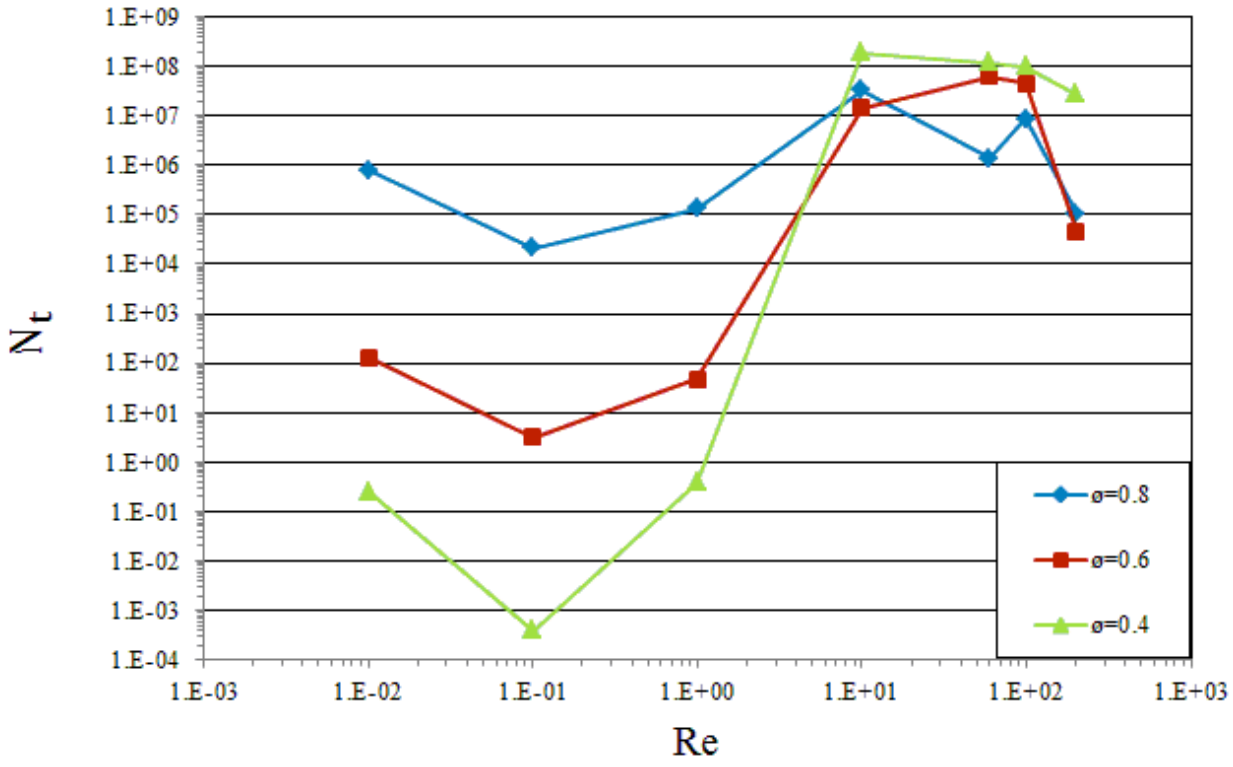

Fig. 11. The N_t variations of circular cross-section configuration for different Reynolds numbers and porosities.

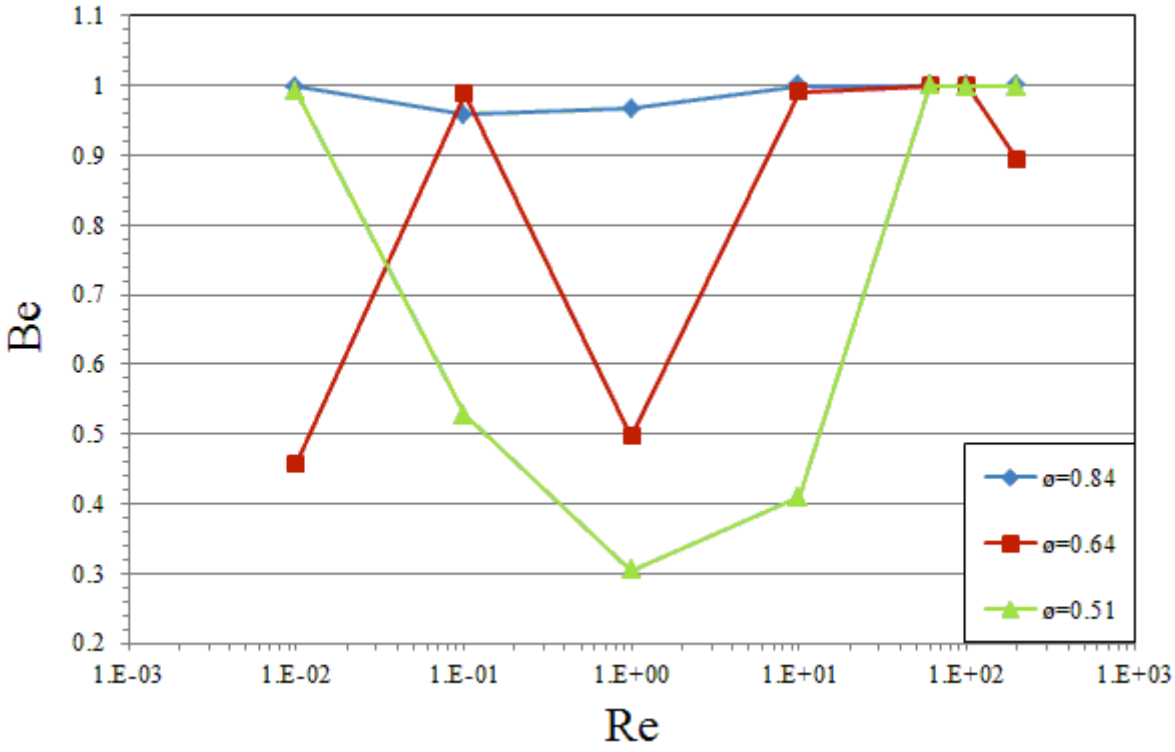

Fig. 12. The *Be* variations of square cross-section configuration for different Reynolds numbers and porosities.

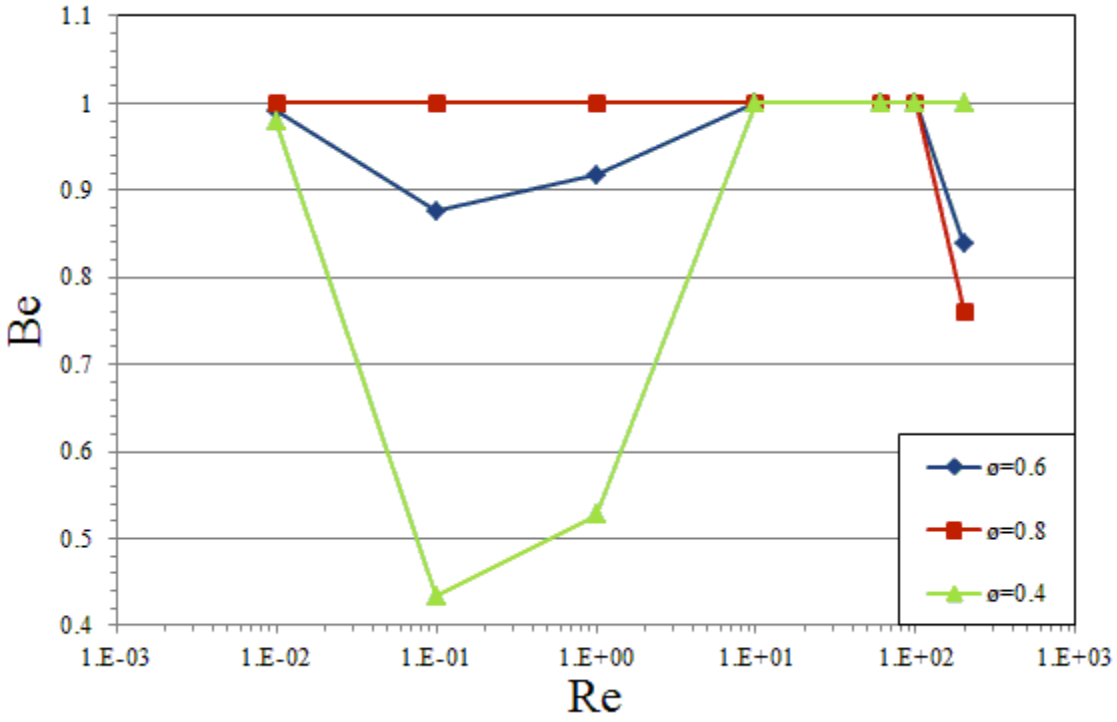

Fig. 13. The *Be* variations of of circular cross-section configuration for different Reynolds numbers and porosities.

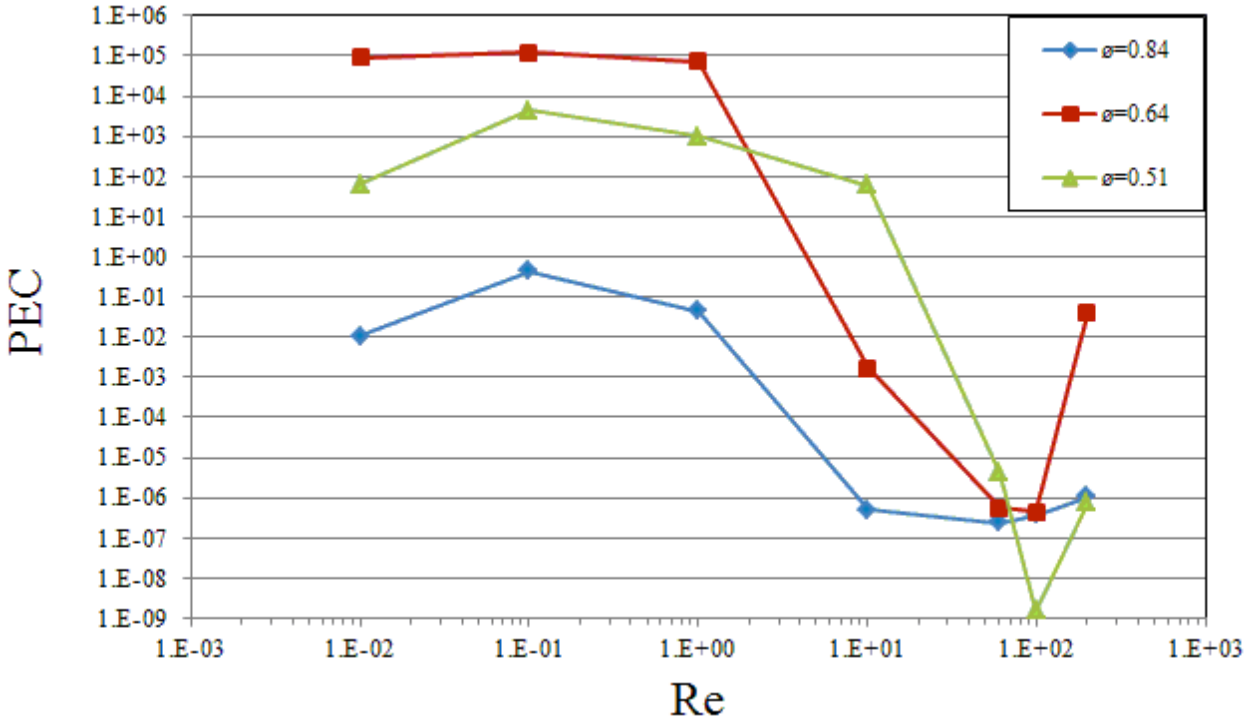

Fig. 14. The PEC variations of square cross-section configuration for different Reynolds numbers and porosities.

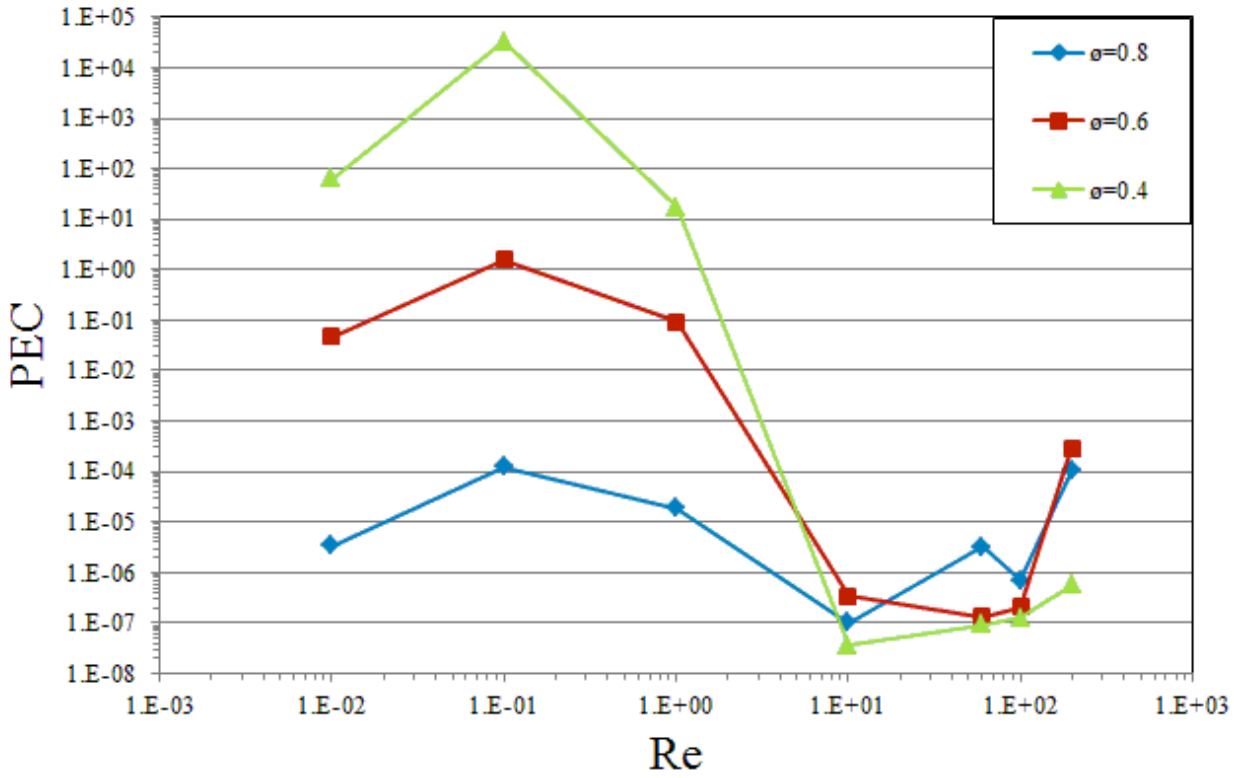

Fig. 15. The PEC variations of circular cross-section configuration for different Reynolds numbers and porosities.

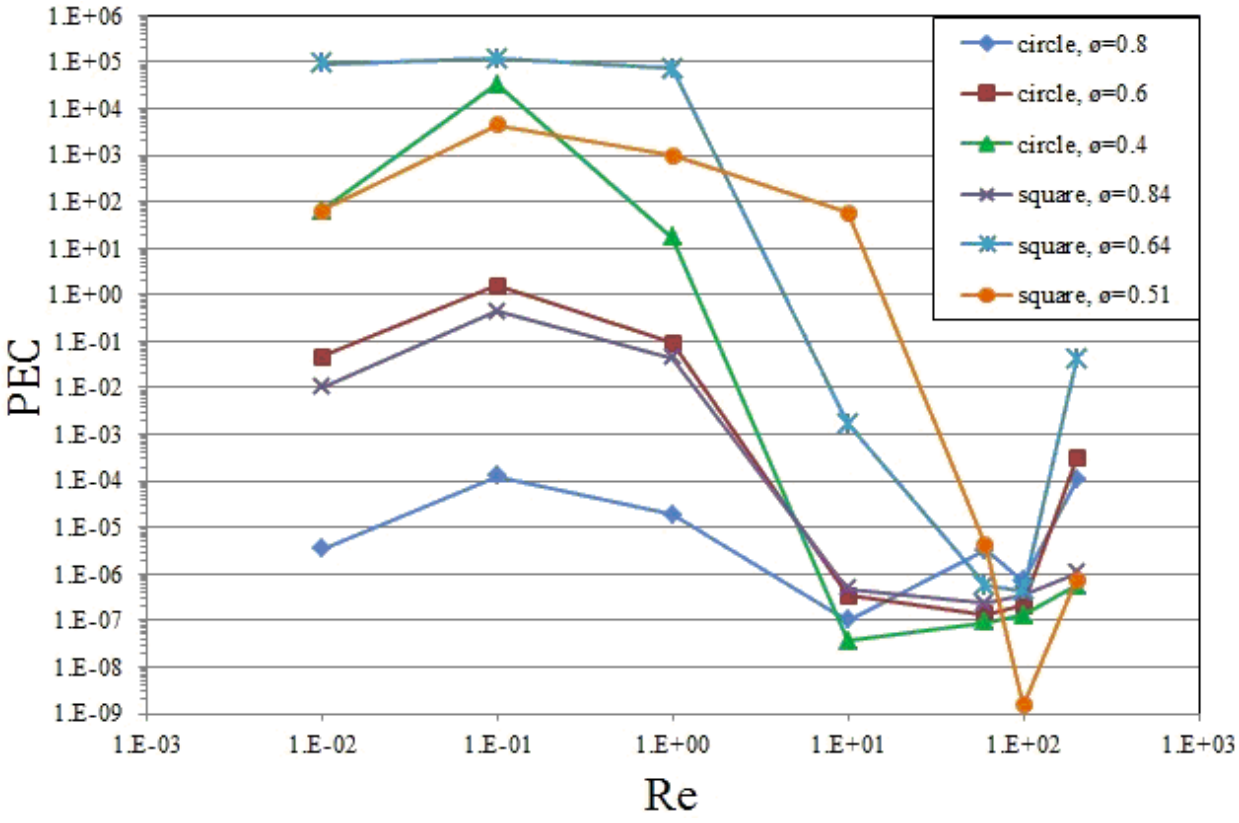

Fig. 16. The PEC variations of circular and square cross-section configurations for different Reynolds numbers and porosities.